

# Potential of Meteosat Third Generation to Detect Water Vapour Convergence Linked to Severe Convection.

Report TN-3: Final Report  
Outcome of Analysis and Recommendations.

This study was performed under EUMETSAT contract. Ref: EUM/PPS/SOW/04/0089

Xiang-Yu Huang\*, Ying-Hwa Kuo and James Done

National Center for Atmospheric Research, US

July 5, 2005

## Abstract

High-resolution numerical simulations of severe convection are examined to determine the relationship between low-level water vapour convergence and severe convection, and to provide guidance as to the optimal repeat cycle of water vapour convergence observations for nowcasting severe weather using Meteosat Third Generation (MTG). For a range of convective situations, low-level water vapour convergence evolves on two timescales; a slow increase on synoptic/mesoscale timescales in the hours before convection followed by a fast increase close to the onset of severe convection. The rapid increase of water vapour (and its associated moisture convergence) can serve as a useful precursor to severe convection. Our results show a significant increase of water vapour convergence occurs prior to severe convection, with lead-times in the range of 20 to 40 minutes. This relationship appears to be quite robust for grid spacing smaller than 30km and temporal interval of 30 minutes or smaller. Based on these results, we conclude that a satellite remote sensing instrument capable of providing a 10 min repeat cycle and at a resolution of 10km would be able to detect significant moisture convergence, and provide useful warning for the possibility of severe convection.

## 1 Background

During the first MTG Mission Team (MMT) meeting 8-9 March 2004, a question was raised whether high spatial and temporal observations of water vapour convergence would increase

---

\*On leave from the Danish Meteorological Institute, Denmark

<i>Imagery Mission</i>	<i>Repeat Cycle</i>	<i>Spatial Resolution</i>
HRFI	5 min	0.5 - 1.0 km
FDHSI	10 min	1.0 - 3.0 km

Table 1: Imagery mission specifications

the lead-time and knowledge of locations for forecasting severe weather. It was argued that the low-level water vapour convergence might be observed about one hour before the onset of severe convection. However, the area covered by the water vapour convergence might be large, so the precise location of severe convection would not be detectable. The other opinion was that very close to the onset of severe convection the area with an increased signal in water vapour convergence could be observed, which would give lead-time for a warning.

Two candidate imagery instruments are proposed for MTG; the High Resolution Fast Imagery (HRFI) and the Full Disk High Spectral Resolution Imagery (FDHSI). Specifications are provided in Table 1. A study on the relation between water vapour convergence and severe convection was proposed to provide recommendations on the optimal repeat cycle for observations of low-level water vapour convergence for nowcasting severe weather. Specifically, the aim of this study is to decide on whether five minute repeat cycles of water vapour convergence observations are needed, or whether ten minute cycles would be sufficient. In this aim, a state-of-the-art non-hydrostatic model is used to simulate several selected cases of severe convection at high spatial and temporal resolution.

This final report presents our recommendations on the optimal repeat cycle of water vapour convergence observations. Some details from previous reports (TN-1, Huang *et al.* (2004) and TN-2, Huang *et al.* (2005)) are included in this report for completeness. Brief descriptions of selected cases of severe convection are provided in section 2, followed by an overview of the numerical modelling system in section 3. Analysis of numerical simulations are presented in sections 4 and 5. Finally, results are summarised and recommendations are given in section 6.

## 2 Selected Case Studies

Cases of severe convection are selected from the period of the the Bow-Echo and Mesoscale Convective Vortex Experiment (BAMEX; Davis *et al.* (2004)). The overarching strategy of BAMEX was to observe the lifecycle of Mesoscale Convective Systems (MCSs), through their organisation, maturation, dissipation and ultimate downstream regeneration. Operations were conducted between mid-May and early July 2003 over the Midwest United States. Throughout this period an array of highly mobile observing platforms (see Davis *et al.* (2004) for details) provided high resolution observational data.

The relationship between water vapour convergence and severe convection may depend on the convective environment and convective-system mode. Therefore, in an attempt to provide a set of cases representing a cross-section of convective environments, three cases are selected,

each of different convective-system mode. Extensive observational data of the cases, including radar and satellite animations, are archived at <http://www.joss.ucar.edu/bamex/catalog>.

Case 1 is the severe bow-echo system<sup>1</sup> observed during 9-10 June 2003. Two tornadic supercells formed over northeast Nebraska around 0000 UTC 10 June along and just ahead of an upper-level wave and associated surface cold front. Two distinct bow structures quickly developed and subsequently consolidated into a continuous line that assumed a storm motion of  $17\text{ms}^{-1}$  towards the southeast ( $128^\circ$ ). The mature bow-echo system is shown in the right panel of Fig. 1. The complete lifecycle of the system took place within a 24 hour period.

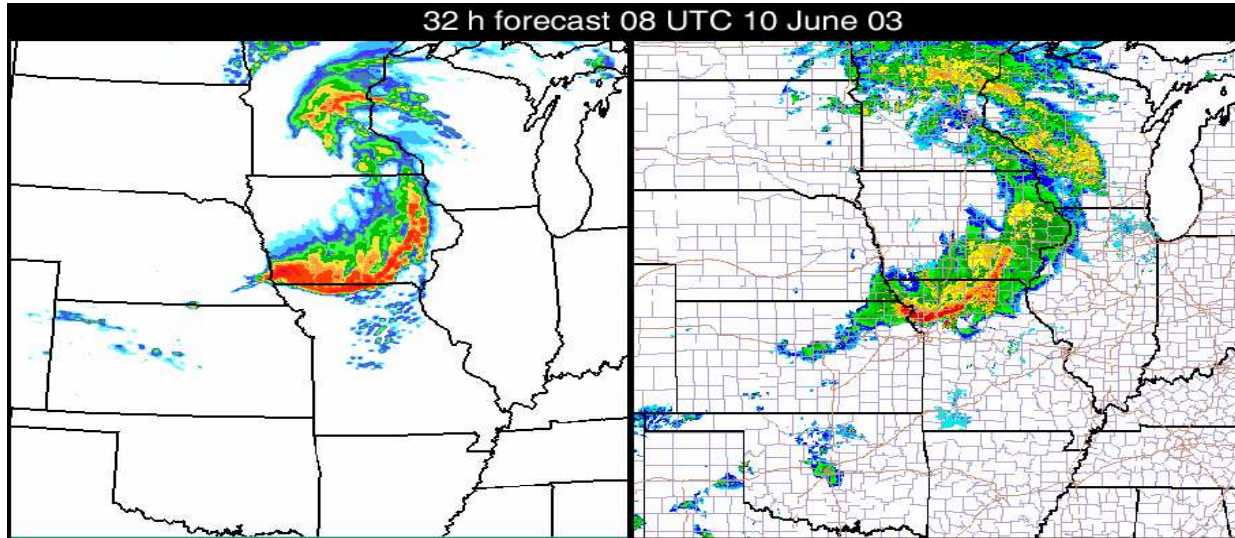


Figure 1: The bow-echo system at 0800 UTC 10 June shown in (right panel) observed maximum reflectivity in each column (2km grid), and (left panel) WRF model derived maximum reflectivity in each grid column (dBZ) from the BAMEX WRF forecast initialised at 0000 UTC 9 June (4km grid).

Case 2 is a line of supercells that tracked across the Great Lakes region on 30th May 2003. An upper-level shortwave trough moved southeastward into the Great Lakes region, and convection was initiated under strong forcing along a trailing cold front south of a surface low. Although instability was weak to moderate, strong shear of the horizontal wind supported supercells. The line of supercells is shown in the right panel of Fig. 2.

The convective system in Case 3 is characterised by a leading line of convective cells and a trailing stratiform region, known as a leading-line MCS. Convection was triggered over Oklahoma and Kansas from 2100 UTC 10 June along a trailing cold front. Whereas the convective environment of case 1 was characterised by weak thermodynamic gradients at low levels, convection for this case was initiated along the strong thermodynamic gradient of the cold front. Convection subsequently organised overnight into a leading-line MCS, shown in the right panel of Fig. 3.

<sup>1</sup>See Fujita (1978) and Weisman (2001) for a description of bow-echo systems.

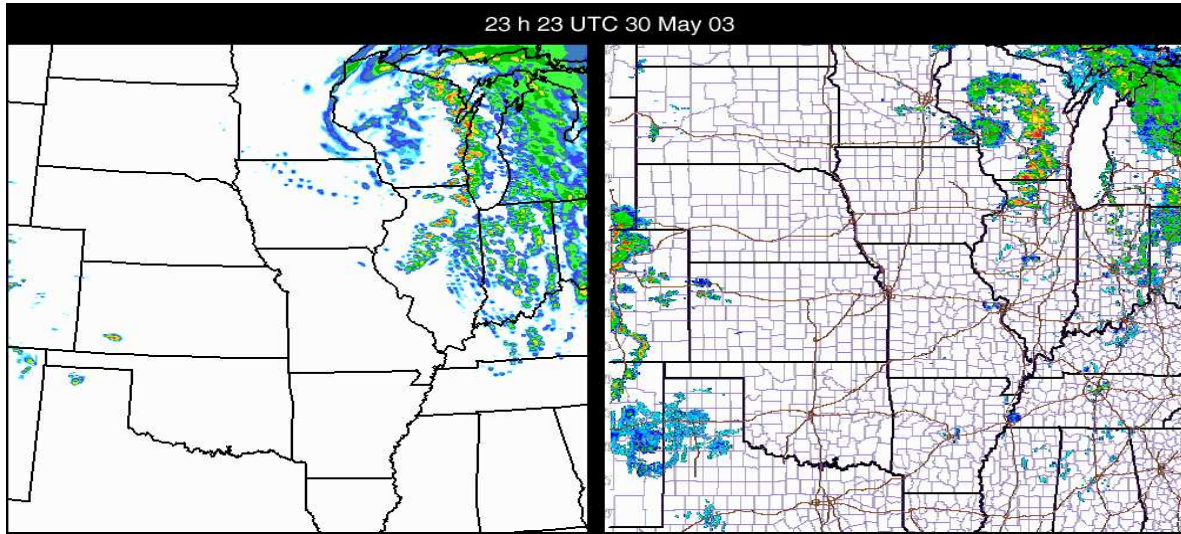


Figure 2: The line of supercell convection at 2300 UTC 30 May shown in (right panel) observed maximum reflectivity in each column (2km grid), and (left panel) WRF model derived maximum reflectivity in each grid column (dBZ) from the BAMEX WRF forecast initialised at 0000 UTC 30 May (4km grid).

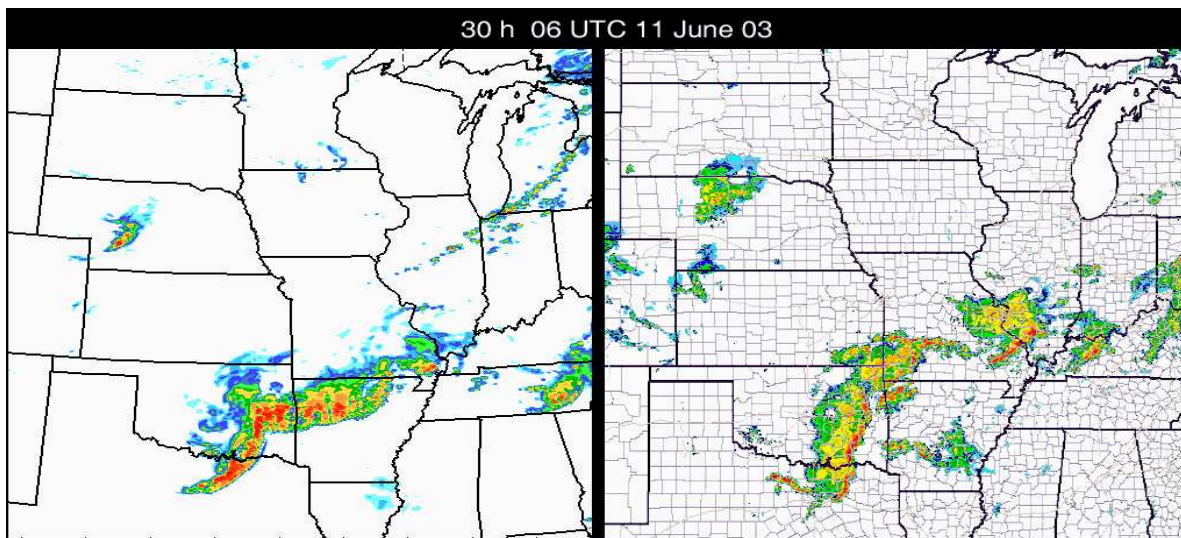


Figure 3: The leading line MCS at 0600 UTC 11 June shown in (right panel) observed maximum reflectivity in each column (2km grid), and (left panel) WRF model derived maximum reflectivity in each grid column (dBZ) from the BAMEX WRF forecast initialised at 0000 UTC 10 June (4km grid).

### 3 The Weather Research and Forecasting (WRF) model

The WRF model (Michalakes *et al.*, 2001) is an advanced mesoscale and data assimilation system designed for cloud and mesoscale (1-10km) applications over a limited area. The

model uses an Eulerian solver based on a flux formulation to solve the fully compressible non-hydrostatic equations that govern the dynamics and thermodynamics of the atmospheric circulation. The Eulerian solver uses a third order Runge-Kutta time integration, third to fifth order advection operators, and split-explicit acoustic/gravity wave integration (Wicker and Skamarock, 2002) conserving both mass and energy. The high-order numerical methods make the WRF model well suited for the high resolution simulations proposed in this study. A suite of physics packages is available to the user, as described at [www.wrf-model.org](http://www.wrf-model.org).

BAMEX provided an unprecedented opportunity to evaluate many WRF model forecasts of severe convection. During the field phase of BAMEX, 36hr real-time forecasts were conducted daily with version 1.3 of WRF using a 4km horizontal grid-spacing over the central United States. Details of the selected physics parameterizations are given in Done *et al.* (2004). A grid-spacing of 4km is considered sufficient to represent MCSs explicitly without the need for a parameterization of convection (Weisman *et al.*, 1997) but is still insufficient for representing many cell-scale processes critical for severe weather forecasting (as discussed in Bryan *et al.* (2003)). Done *et al.* (2004) showed these explicit convection forecasts were able to accurately predict the number of MCSs daily, the convective-system mode and evolution of the MCSs. Examples of useful WRF forecasts are shown for the three selected cases in the left panels of Figs. 1, 2 and 3 together with observations shown in the right panels. WRF forecasts during BAMEX are archived at <http://www.joss.ucar.edu/bamex/catalog>.

### 3.1 Model Setup

The model setup is similar to that of the real-time BAMEX WRF forecasts. However, for this study, the recently released Version 2.0.3 of the WRF model is used with one-way nesting. All domains have 35 terrain-following levels specified in the vertical, spaced roughly 250m apart in the lowest km with monotonic stretching to about 1km spacing near and above 14km. The model top is at 50hPa. The basic physics packages are the same for both domains and include the Mellor-Yamada-Janjic (ETA) boundary layer scheme, the Noah land surface model, and the Lin microphysics scheme with 6 prognostic moisture variables (derived from the original scheme described in Lin *et al.* (1983)). Second-order diffusion is applied in the horizontal, and damping is applied to vertical velocity. Convective parameterization is not used and no additional data are assimilated.

The parent domain used for all simulations is shown in Fig. 4 together with the 3 nested domains. The parent domain of  $500 \times 500$  grid points uses 4km horizontal grid-spacing. Initial and boundary conditions are derived from the 40km ETA analyses available at 3 hourly intervals. Boundary conditions at each timestep are interpolated between the 3 hourly ETA analyses. The parent domain communicates with the nested domain by providing boundary conditions at each timestep. Nested domains of approximately  $600 \times 500$  grid points use 1km horizontal grid-spacing, and are located such that convection initiates close to the centre of the domain. Both parent and nested domains are initialised using the ETA analyses, approximately six hours prior to the observed initiation of convection. Simulations run for 12 hours and capture the pre-convective environment, convection initiation and subsequent mesoscale convective organisation. This allows for study of the evolution of the water vapour

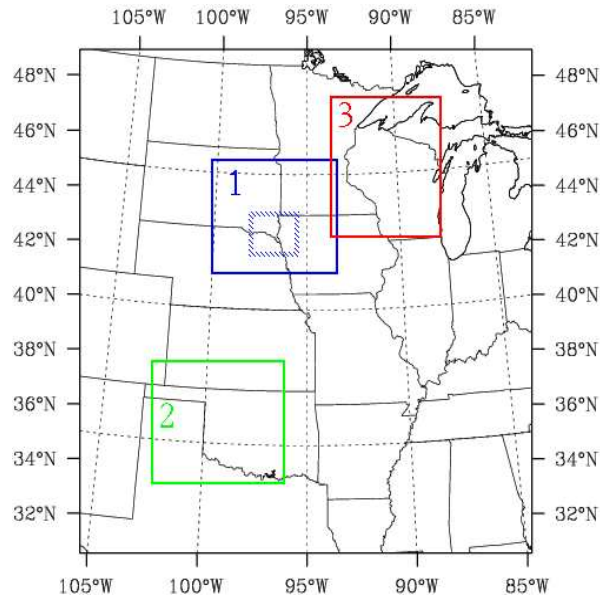


Figure 4: The parent domain and nested domains for case 1 (blue), case 2 (green) and case 3 (red). Outlined in a blue dashed line is a sub-region of the nested domain for case 1 used to calculate area average quantities.

field prior to convection and to determine the relationship, if any, between water vapour convergence and severe convection. Data from the nested domain are archived every minute. The archived variables are:

- 3D time rate of change of water vapour
- 3D water vapour divergence
- 3D potential temperature
- 3D water vapour mixing ratio
- 3D cloud water mixing ratio
- Vertically integrated water vapour for the layers: surface-800mb; surface-700mb; 800-500mb; 700-300mb; 500-50mb and 300-50mb.
- Precipitable water
- Accumulated explicit precipitation
- Temperature at 2m
- Surface (skin) temperature

## 4 Analysis of Case 1: Bow-Echo System, 9-10 June 2003

The simulation of case 1 captured the initiation of convection close to the center of the nested domain at approximately 0130 UTC 10 June 2003. Model convection quickly organised into a propagating bow-echo system, as observed. Further convection initiated within the nested domain and subsequently merged with the bow-echo system. Figure 5 shows the evolution of the model bow echo system within the sub-region of the nested domain outlined in Fig. 4. This sub-region is used later to calculate area averaged quantities and to isolate the water vapour signature associated with the bow-echo system. The sub-region includes the pre-convective environment, initiation and organisation of the bow-echo.

### 4.1 Relationship with Water Vapour Convergence

Following Kuo (1974), low-level water vapour convergence is defined as;

$$- \int \rho \nabla \cdot (q \mathbf{V}_h) dZ, \quad (1)$$

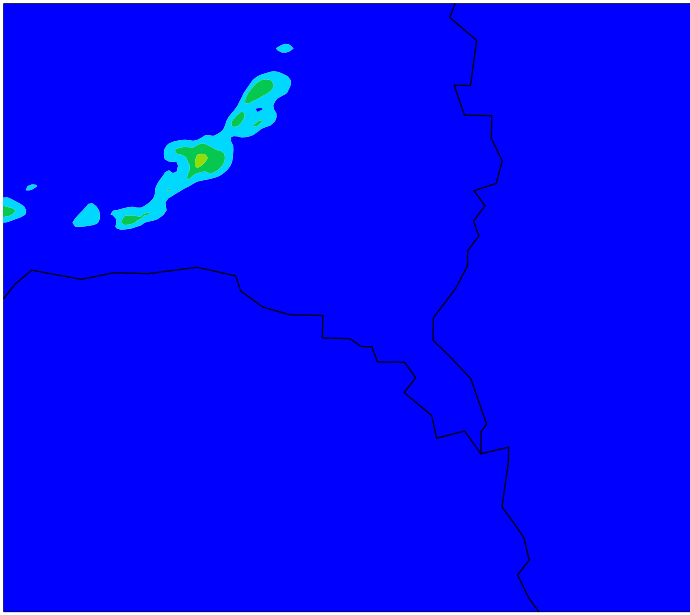
where  $\rho$  is density,  $q$  is water vapour mixing ratio,  $\mathbf{V}_h$  is the 2-dimensional wind field and  $Z$  is geopotential height. *Low-level* is defined here as the depth of the boundary layer of the convective environment. A vertical profile ahead of the propagating bow-echo, shown in Fig. 6, obtained from a dropsonde released at 0349 UTC 10 June shows the top of the boundary layer at approximately 800mb.

Figure 7a shows a timeseries of low-level water vapour convergence and 1 minute accumulated rainfall, averaged over the sub-region. 1-minute rainfall amount is used here as a proxy for convection. Water vapour convergence appears to evolve on two timescales; a slow increase in the hours before convection followed by a fast increase close to the onset of convection. This suggests mechanisms are operating on two timescales; the slow increase associated with the synoptic/mesoscale development of the convective environment and the fast increase associated with a precursor mechanism to convection. This suggests a relationship between low-level water vapour convergence and severe convection.

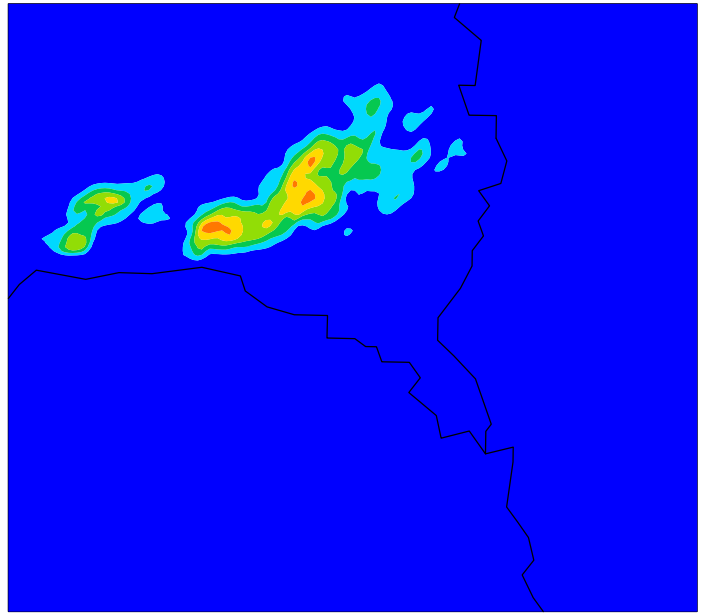
MTG does not observe low-level water vapour convergence as defined in Eqn. 1 since it does not observe winds. For the purposes of this study, it is assumed that MTG observes only total column water vapour, known as Precipitable Water (PW). Additional assumptions are made that the time tendency of PW provides an estimate for low-level water vapour convergence, and that the discrete time rate of change of PW approximates the time derivative. Therefore it is assumed that MTG uses the time rate of change of PW as a proxy for the vertically integrated water vapour convergence. The two fields are not the same and may behave quite differently.

PW is defined as;

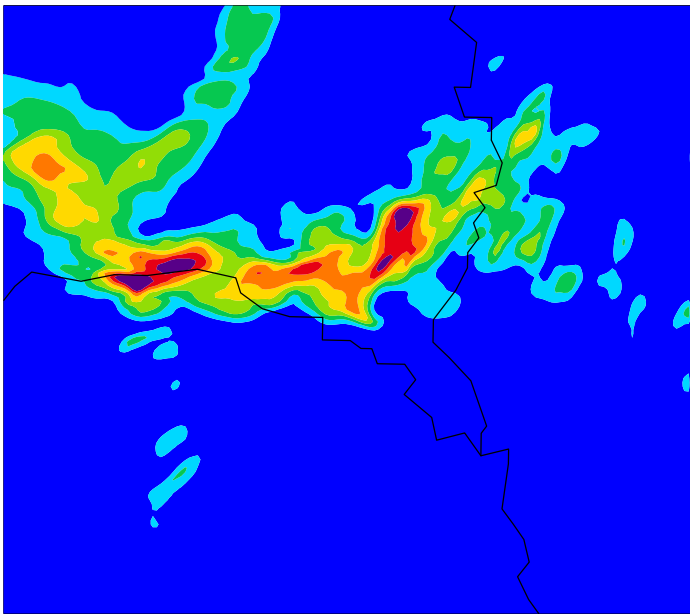
A 0145-0200 UTC



B 0245-0300 UTC



C 0345-0400 UTC



D 0445-0500 UTC

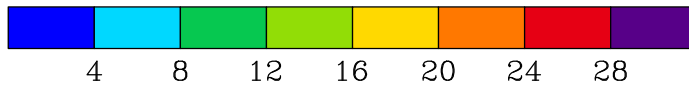
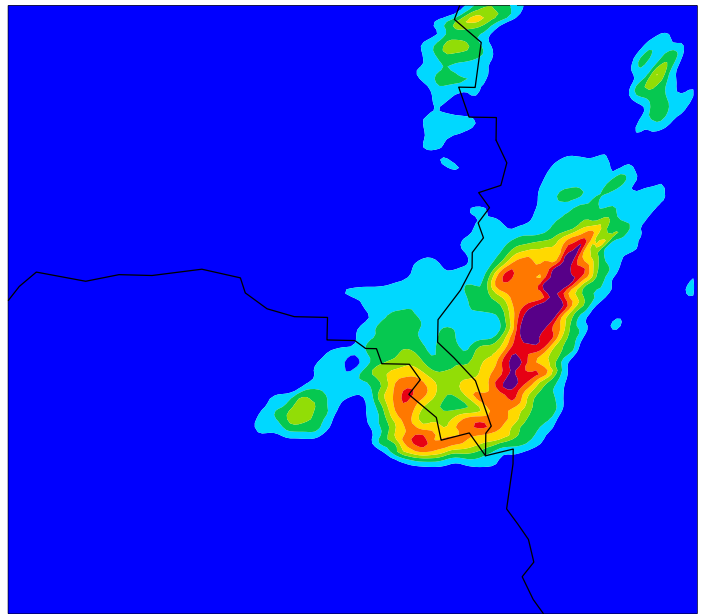


Figure 5: 15-minute accumulated rainfall (mm) shown for the sub-region of the nested domain for the periods (a) 0145-0200 UTC, (b) 0245-0300 UTC, (c) 0345-0400 UTC and (d) 0445-0500 UTC 10 June 2003.

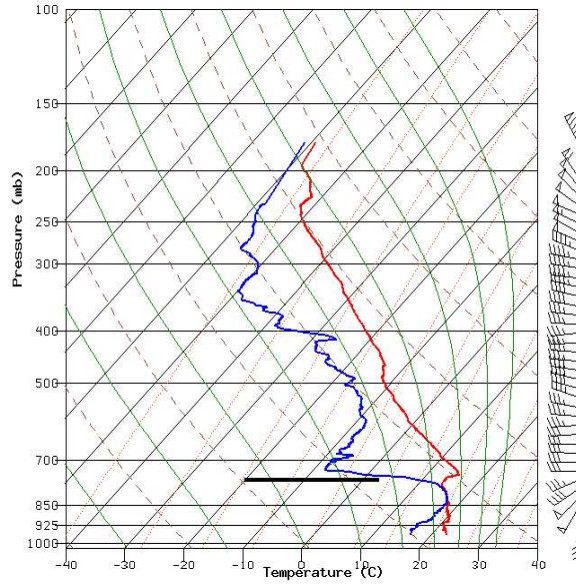


Figure 6: Observed vertical profile of temperature (red), dew-point temperature (blue) and wind speed and direction (wind barbs) at 0349 UTC 10 June 2003. The thick black line marks the top of the convective boundary layer.

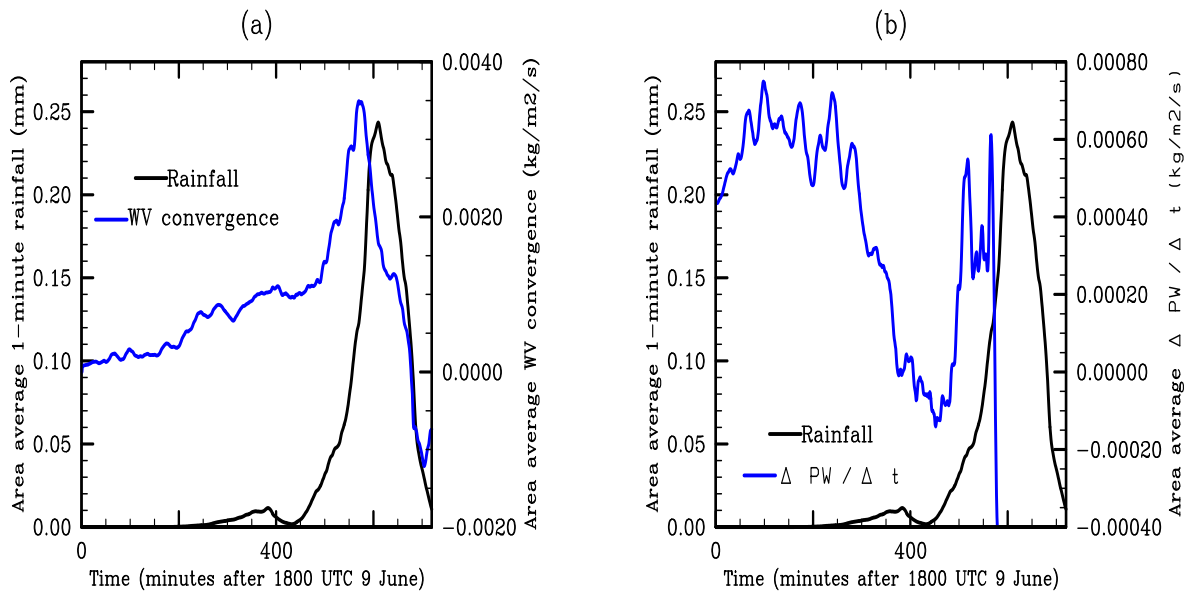


Figure 7: (a) Timeseries of 1-minute rainfall accumulation (mm, black) and low-level water vapour convergence ( $\text{kgm}^{-2}\text{s}^{-1}$ , blue), and (b) Timeseries of 1-minute rainfall accumulation (mm, black) and time rate of change of PW using  $\Delta t = 1\text{min}$  ( $\text{kgm}^{-2}\text{s}^{-1}$ , blue). All quantities are area averages taken over the sub-region.

$$\int \rho q dZ. \quad (2)$$

Therefore, the time rate of change of total column water vapour can be expressed as;

$$\frac{\partial PW}{\partial t} = \int \rho \frac{\partial q}{\partial t} dZ. \quad (3)$$

We know that;

$$\frac{\partial q}{\partial t} + \mathbf{V} \cdot \nabla q = Q, \quad (4)$$

where  $\mathbf{V}$  is the 3d wind field and  $Q$  represents the sources and sinks of water vapour mixing ratio. Rearranging Eqn. 4 for  $\frac{\partial q}{\partial t}$  and combining with Eqn 3 gives;

$$\frac{\partial PW}{\partial t} = \int \rho Q dZ - \int \rho \mathbf{V} \cdot \nabla q dZ, \quad (5)$$

and it follows that;

$$\frac{\partial PW}{\partial t} = \int \rho Q dZ - \int \rho \nabla \cdot \mathbf{V} q dZ + \int \rho q \nabla \cdot \mathbf{V} dZ. \quad (6)$$

The time rate of change of PW therefore depends on the source/sink terms, the vertically integrated 3d water vapour convergence and a 3d mass convergence term. The time rate of change of PW and vertically integrated water vapour convergence are therefore not the same quantity.

Figure 7b shows timeseries of the time rate of change of PW using  $\Delta t = 1$  minute and 1 minute accumulated rainfall, both averaged over the sub-region. As for low-level water vapour convergence,  $\Delta PW / \Delta t$  evolves on two timescales; a slow increase on synoptic/mesoscale timescales in the hours before convection followed by a fast increase close to the onset of severe convection. This suggests a relationship between  $\Delta PW / \Delta t$  and severe convection.

## 4.2 Lead-Times of the Precursors to Severe Convection

Precursors to severe convection have been identified in the time-series of low-level water vapour convergence and  $\Delta PW / \Delta t$ . Knowledge of the lead-time of the precursor is useful for nowcasting purposes. An estimate for the lead-times can be obtained by correlating the

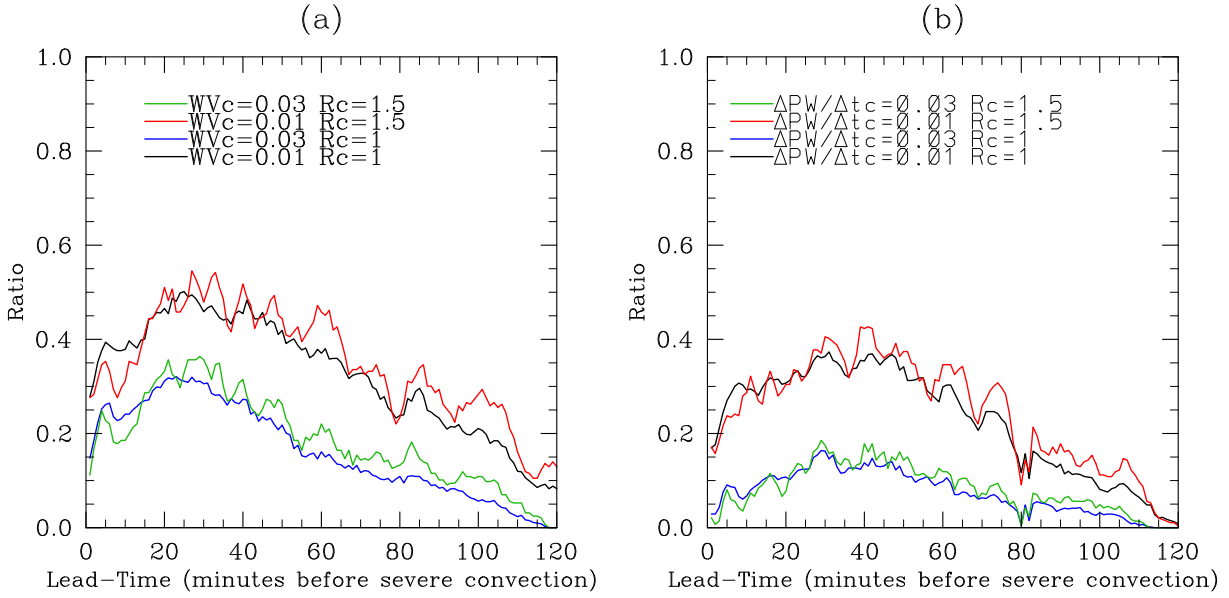


Figure 8: Ratio of the number of grid points exceeding a rainfall threshold to the number of those grid point exceeding (a) a water vapour convergence threshold and (b) a  $\Delta PW / \Delta t$  threshold, for different thresholds.

1-minute rainfall field with either the water vapour convergence field or the  $\Delta PW / \Delta t$  field. Ratio  $Y$  is calculated as follows;

$$Y(t) = \frac{R(n)}{W(n-t)}, \quad (7)$$

where  $R$  is the number of grid points exceeding a 1-minute rain amount threshold ( $R_c$ ) at the time of the onset of severe convection  $n$ . For this case,  $n = 560$  minutes into the simulation.  $W$  is the number of those grid points that exceed a low-level water vapour convergence threshold ( $WV_c$ ) at different lead times  $t$ . To obtain the ratio for  $\Delta PW / \Delta t$ , the low-level water vapour convergence field is substituted for the  $\Delta PW / \Delta t$  field. In converting the fields to binary, dependence on the magnitude is removed, and the ratio becomes a measure of overlap between shapes in the rainfall and water vapour convergence or  $\Delta PW / \Delta t$  fields.

Figure 8a shows the ratio  $Y$  as a function of lead-time,  $t$ , for different values of the tunable threshold parameters  $R_c$  and  $WV_c$ . The shape of the timeseries are not sensitive to the threshold parameters, and maximum ratios occur around 30 minutes lead-time for low-level water vapour convergence. Figure 8b shows the maximum ratios for  $\Delta PW / \Delta t$  occur around 40 minutes.

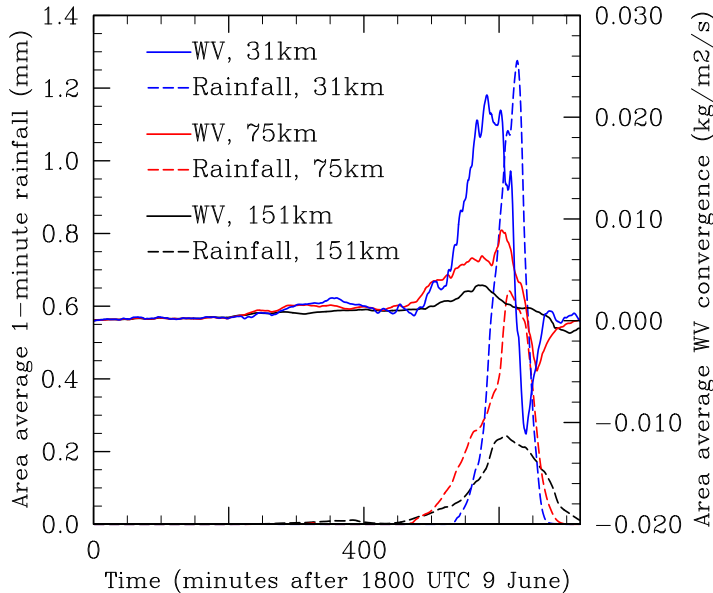


Figure 9: Timeseries of 1-minute rainfall accumulation (mm, dashed) and low-level water vapour convergence ( $\text{kgm}^{-2}\text{s}^{-1}$ , solid) averaged over square boxes of length 151km (black), 75km (red) and 31km (blue).

### 4.3 Sensitivity to Averaging Area

A precursor to severe convection has been identified in low-level water vapour convergence on the scale of the sub-region averaging area ( $151\text{km} \times 151\text{km}$ ). For nowcasting purposes it is desirable to detect precursors over smaller spatial scales to be more precise on the location for severe weather warnings. Here, the sensitivity of characteristics of the precursor to the averaging area are examined.

Figure 9 shows timeseries of area averaged low-level water vapour convergence and 1 minute accumulated rainfall for three averaging areas;  $151\text{km} \times 151\text{km}$ ,  $75\text{km} \times 75\text{km}$  and  $31\text{km} \times 31\text{km}$ . The center grid-point for all averaging areas is the same, resulting in box lengths of uneven number of grid spacings. A precursor is present for all averaging area sizes, and the time of the peak magnitude in water vapour convergence has low sensitivity to the averaging area size. As the averaging area is reduced, the magnitude of the area-averaged quantities increases, since the center point lies approximately at the location of highest rainfall amount. Similar results are found for the precursor in  $\Delta PW / \Delta t$  (not shown).

### 4.4 Sensitivity to Temporal and Spatial Resolution

The candidate imagery missions HRFI and FDHSI have different spatial and temporal observing capabilities, as shown earlier in Table 1. To determine the choice of repeat cycle (and therefore spatial resolution) of low-level water vapour observations for nowcasting severe weather, the sensitivity of the precursor in low-level water vapour convergence to the spatial

and temporal resolution of the data is examined.

Figure 10 shows no significant differences in the timeseries of area average water vapour convergence using different spatial and temporal resolution data (for the range relevant to this study; 1km - 30 km and 1 min to 30 min) for an averaging area of 31km $\times$  31km. This result is independent of the averaging area size for square boxes with side lengths between 31km and 151km (not shown). Changes occur on timescales of 30 minutes or greater and spatial scales of 30km or greater, resulting in low sensitivity of the magnitude and 'shape' of the precursor to the range of spatial and temporal resolutions relevant to this study; 1km - 30 km and 1 min to 30 min. Therefore, observations with a horizontal resolution of 3km using a repeat cycle of 10 minutes (e.g. FDHSI) properly describes the time evolution of low-level water vapour. Similar results are found for the precursor in  $\Delta PW / \Delta t$  (not shown).

## 5 Analysis of Case 2: Line of Supercells, 30 May 2003 and Case 3: Leading-Line MCS, 10 June 2003

Similar analysis as for case 1 has been performed for cases 2 and 3, and brief overviews are provided here.

Simulations of cases 2 and 3 both captured the approximate location and timing of convection initiation close to the centre of the nested domains, and captured the observed convective mode; a line of supercells for case 2, and a leading line MCS for case 3. The numerical simulation data are therefore adequate to investigate the relationship between water vapour convergence and severe convection.

As for case 1, simulations of cases 2 and 3 show fast increases in area averaged low-level water vapour convergence (shown in Fig. 11) and  $\Delta PW / \Delta t$  (not shown) prior to severe convection. Again, these precursors suggest a relationship with severe convection. Using a similar correlation technique as for case 1, maximum correlations between the field of 1-minute rainfall and either water vapour convergence or  $\Delta PW / \Delta t$  occur around lead-times of 20 minutes for case 2 and 30 minutes for case 3. In addition, characteristics of the precursors, such as the 'shape' and lead-time, have low sensitivity to the size of the averaging area (not shown), and to the spatial and temporal resolutions of the data for the ranges relevant to this study; 1km - 30 km and 1 min to 30 min (shown in Figs 12 and 13 for box averages of size 31km).

## 6 Summary and Recommendations

For a range of convective situations, low-level water vapour convergence and the time tendency of PW evolves on two timescales; a slow increase on synoptic/mesoscale timescales in the hours before convection followed by a fast increase close to the onset of severe convection. The rapid increase of water vapour (and its associated moisture convergence) can serve as a

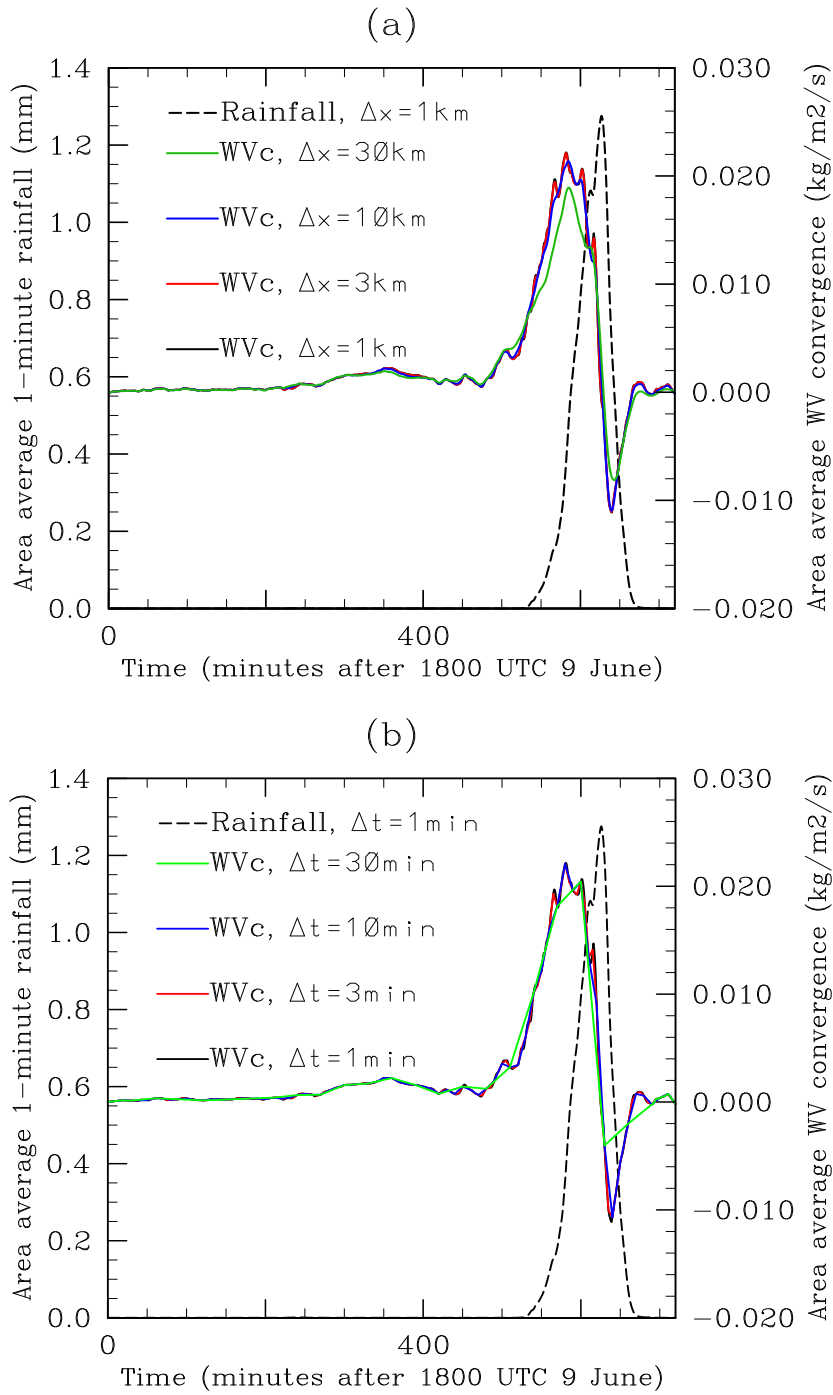


Figure 10: Timeseries of 1-minute rainfall accumulation (mm, dashed) and low-level water vapour convergence ( $\text{kgm}^{-2}\text{s}^{-1}$ , solid) averaged over a 31km square box using (a) data of degraded spatial resolution and (b) data of degraded temporal resolution.

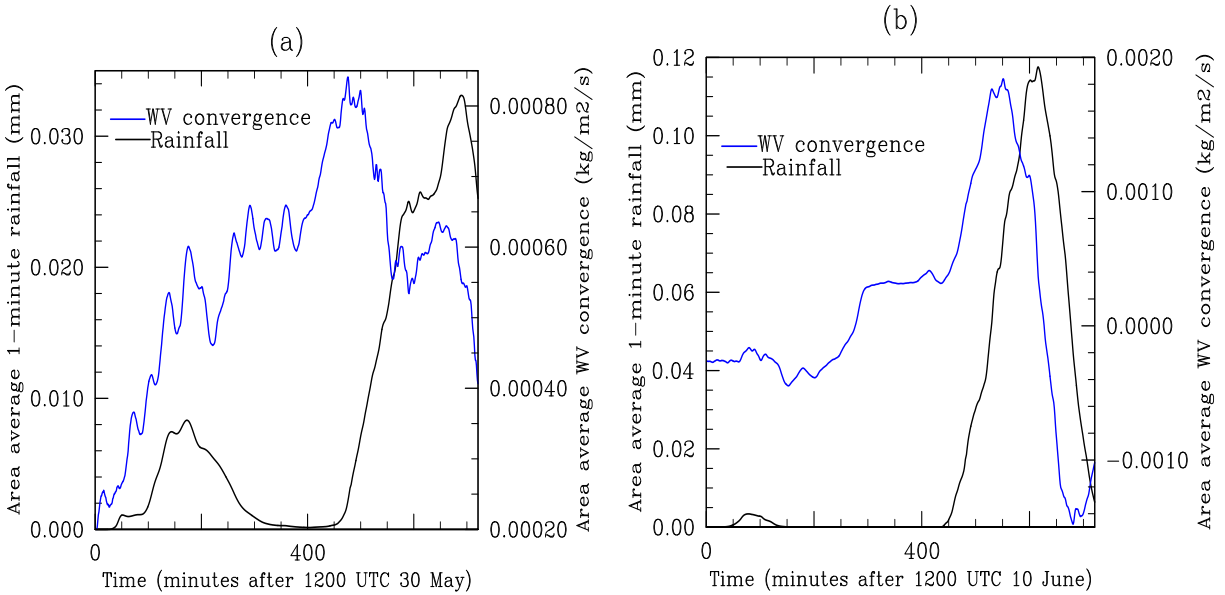


Figure 11: Timeseries of 1-minute rainfall accumulation (mm, black) and low-level water vapour convergence ( $\text{kgm}^{-2}\text{s}^{-1}$ , blue) averaged over a 151km square box for (a) case 2 and (b) case 3.

useful precursor to severe convection. Our results show a significant increase of water vapour convergence occurs prior to severe convection, with lead-times in the range of 20 to 40 minutes. This relationship appears to be quite robust for grid spacing smaller than 30km and temporal interval of 30 minutes or smaller.

Based on these results, we conclude that a satellite remote sensing instrument capable of providing a 10 min repeat cycle and using a spatial resolution of 3km (as proposed by FDHSI) properly describes the time-evolution of water vapour, and would provide useful warning for the possibility of severe convection.

## References

- Bryan, G., Wyngaard, J., and Fritsch, J. (2003). Resolution requirements for the simulation of deep moist convection. *Mon. Wea. Rev.*, **131**, 2394–2416.
- Davis, C., Atkins, N., Bartels, D., Bosart, L., Coniglio, M., Bryan, G., Cotton, W., Dowell, D., Jewett, B., Johns, R., Jorgenson, D., Knievel, J., Knupp, K., Lee, W.-C., McFarquar, G., Moore, J., Pryzbylinski, R., Rauber, R., Smull, B., Trapp, R., Trier, S., Wakimoto, R., Weisman, M., and Ziegler, C. (2004). The Bow-Echo and MCV Experiment (BAMEX): Observations and opportunities. *Bull. Amer. Meteor. Soc.*, **85**, 1075–1093.
- Done, J., Davis, C., and Weisman, M. (2004). The next generation of NWP: Explicit forecasts of convection using the weather research and forecasting (WRF) model. *Atmos.*

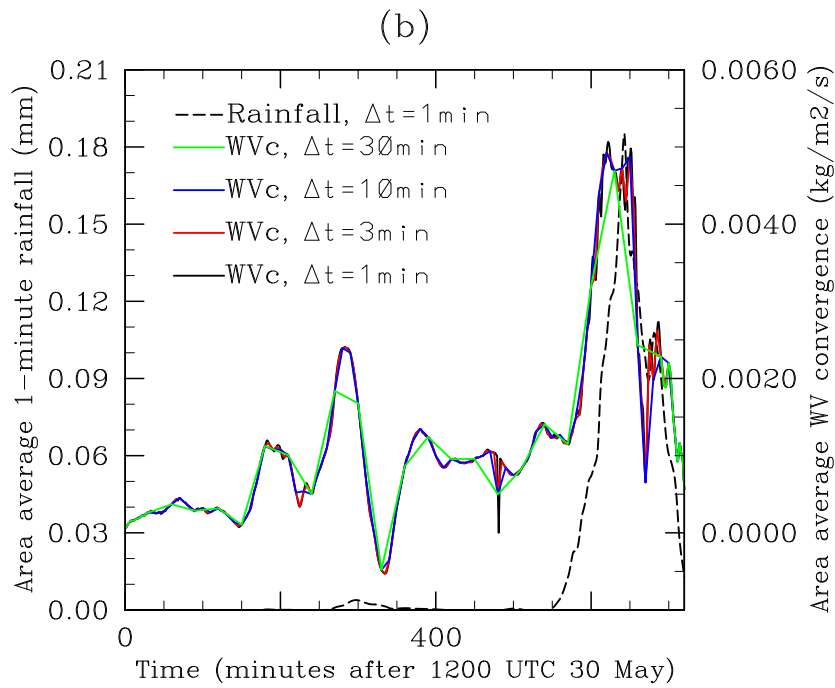
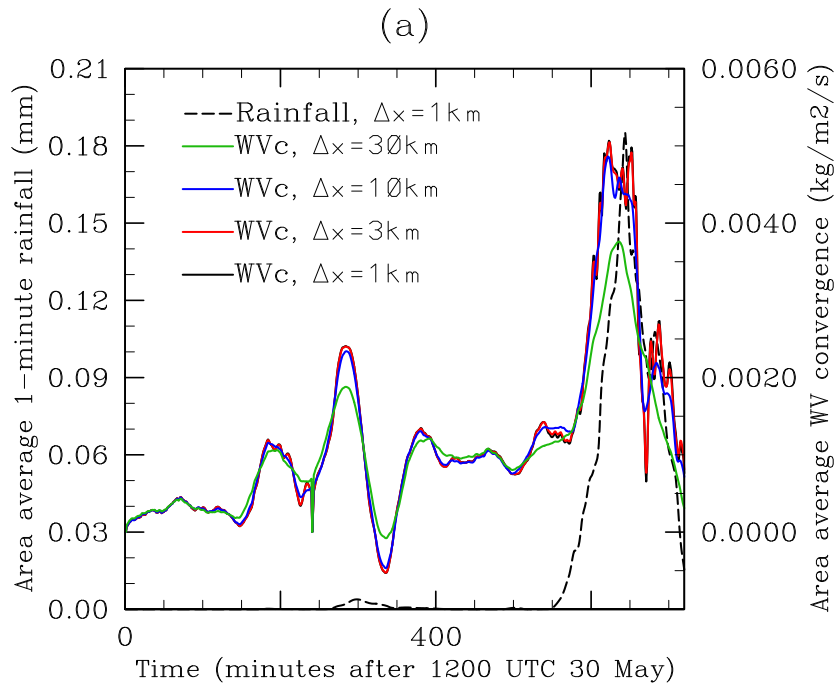


Figure 12: As for Fig. 10 but for case 2.

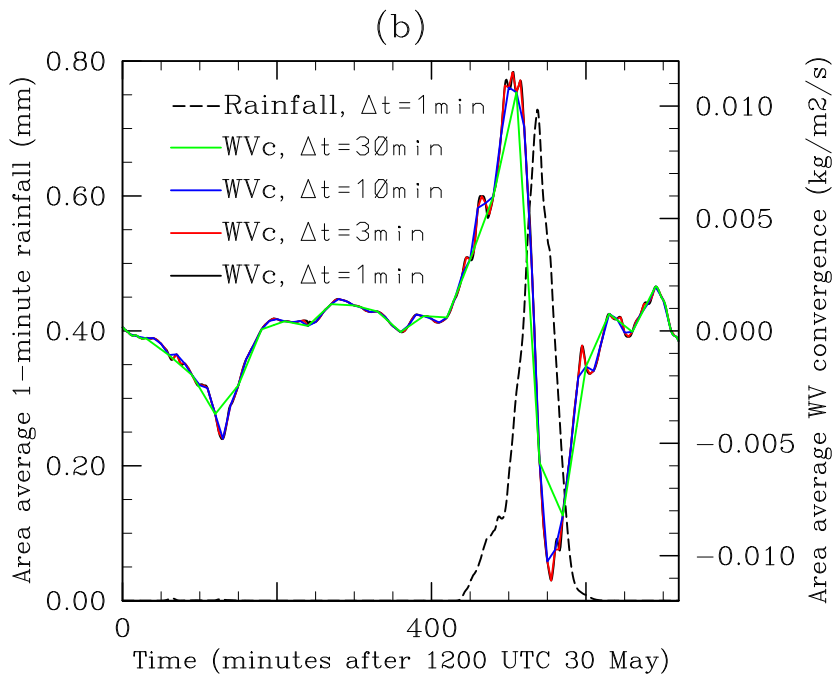
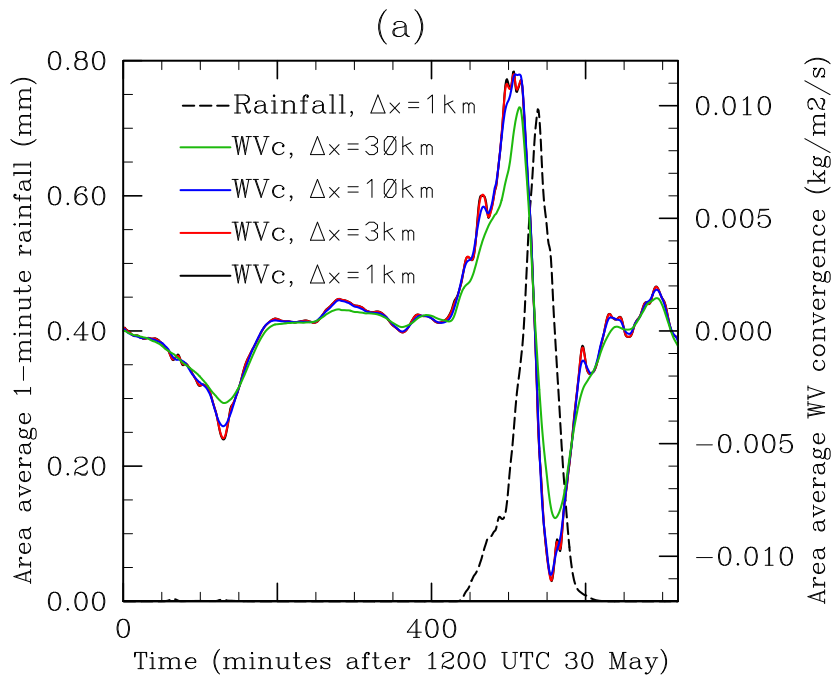


Figure 13: As for Fig. 10 but for case 3.

*Sci. Letters.*, **5**, 110–117.

Fujita, T. (1978). Manual of downburst identification for project NIMROD. In *Satellite and Mesometeorology Research Paper*, number 156, page 104 pp. Department of Geophysical Sciences, University of Chicago.

Huang, X.-Y., Kuo, Y.-H., and Done, J. (2004). Report TN-1: Summary of model setup and selected cases. Eumetsat Report TN-1.

Huang, X.-Y., Kuo, Y.-H., and Done, J. (2005). Report TN-2: Mid-term report summarising preliminary results. Eumetsat Report TN-2.

Kuo, H.-L. (1974). Further studies of the parameterization of the influence of cumulus convection on the large-scale flow. *J. Atmos. Sci.*, **31**, 1231–1240.

Lin, Y.-L., Farley, R., and Orville, H. (1983). Bulk parameterisation of the snow field in a cloud model. *J. Clim. Appl. Meteorol.*, **22**, 1065–1092.

Michalakes, J., Chen, S., Dudhia, J., Hart, L., Klemp, J., Middlecoff, J., and Skamarock, W. (2001). Development of a next generation regional weather research and forecast model. In *Developments in Teracomputing: Proceedings of the Ninth ECMWF Workshop on the Use of High Performance Computing in Meteorology*, Zweifelhofer W, Krietz N(eds)., pages 269–276. World Scientific: Singapore.

Weisman, M. (2001). Bow echoes: A tribute to T. T. Fujita. *Bull. Amer. Meteor. Soc.*, **82**, 97–116.

Weisman, M., Skamarock, W., and Klemp, J. (1997). The resolution dependence of explicitly modeled convective systems. *Mon. Wea. Rev.*, **125**, 527–548.

Wicker, L. and Skamarock, W. (2002). Time-splitting methods for elastic models using forward time schemes. *Mon. Wea. Rev.*, **130**, 2088–2097.